Journal of Solid State Chemistry 205 (2013) 225–235

Contents lists available at ScienceDirect

Journal of Solid State Chemistry

journal homepage: www.elsevier.com/locate/jssc

Lifting the geometric frustration through a monoclinic distortion in "114" $YBaFe_4O_{7.0}$: Magnetism and transport

V. Duffort [a], T. Sarkar [a], V. Caignaert [a,*], V. Pralong [a], B. Raveau [a], M. Avdeev [b], A. Cervellino [c], J.C. Waerenborgh [d], E.V. Tsipis [d]

[a] CRISMAT, CNRS-ENSICAEN, 6 Bd Marechal Juin, 14050 Caen, France
[b] Bragg Institute, Australian Nuclear Science and Technology Organization, PMB 1, Menai, NSW 2234, Australia
[c] Paul Scherrer Institute, Swiss Light Source, CH-5232 Villigen, Switzerland
[d] UCQR, IST/ITN, Instituto Superior Técnico, Universidade Técnica de Lisboa, CFMC-UL, 2686-953 Sacavém, Portugal

ARTICLE INFO

Article history:
Received 1 March 2013
Received in revised form
21 May 2013
Accepted 3 June 2013
Available online 10 July 2013

Keywords:
"114" Iron oxides
Mode crystallography
Magnetic structure
Transport properties

ABSTRACT

The possibility to lift the geometric frustration in the "114" stoichiomeric tetragonal oxide $YBaFe_4O_{7.0}$ by decreasing the temperature has been investigated using neutron and synchrotron powder diffraction techniques. Besides the structural transition from tetragonal to monoclinic symmetry that appears at $T_S = 180$ K, a magnetic transition is observed below $T_N = 95$ K. The latter corresponds to a lifting of the 3D geometric frustration toward an antiferromagnetic long range ordering, never observed to date in a cubic based "114" oxide. The magnetic structure, characterized by the propagation vector $k_1 = (0,0,½)$, shows that one iron Fe2 exhibits a larger magnetic moment than the three others, suggesting a possible charge ordering according to the formula $YBaFe^{3+}Fe_3^{2+}O_{7.0}$. The magnetic $M(T)$ and $\chi'(T)$ curves, in agreement with neutron data, confirm the structural and magnetic transitions and evidence the coexistence of residual magnetic frustration. Moreover, the transport measurements show a resistive transition from a thermally activated conduction mechanism to a variable range hopping mechanism at $T_S = 180$ K, with a significant increase of the dependence of the resistivity *vs.* temperature. Mössbauer spectroscopy clearly evidences a change in the electronic configuration of the iron framework at the structural transition as well as coexistence of several oxidation states. The role of barium underbonding in these transitions is discussed.

1. Introduction

The large family of "114" cobaltites whose prototype, $YBaCo_4O_{7+\delta}$ was first discovered [1], has drawn a lot of attention to the whole series of isotypic $LnBaCo_4O_{7+\delta}$ oxides, where Ln is a lanthanide or Ca^{2+}, which has been explored for its attractive magnetic properties, especially the competition between magnetic ordering and frustration [2–11]. The structure of these compounds, built up of triangular and kagome layers of $[CoO_4]$ tetrahedra, is based on an "ABAC" double hexagonal close packing of "BaO_3" and "O_4" layers forming the "BaO_7" framework [12]. The oxygen stoichiometric samples, $LnBaCo_4O_{7.0}$ ($\delta = 0$) have demonstrated interesting structural transitions *vs.* temperature [2,4,8,10,13,14]. The hexagonal ($P6_3mc$) or trigonal ($P31c$) (depending on authors) high temperature cell is distorted into an orthorhombic ($Pbn2_1$) and eventually to a monoclinic cell ($P2_1$) as reported for $YBaCo_4O_7$ [2] as the temperature is decreased. It is the possibility of transition between these forms, which governs the magnetic properties of these oxides, as for example the lifting of the 2D geometric frustration in the hexagonal oxides by introducing an orthorhombic distortion.

The investigation of "114" mixed valent Fe(II)–Fe(III) oxides has also shown the possibility to synthesize oxides with a closely related structure to the cobaltites, but whose "BaO_7" framework is, differently based on an "ABC" cubic close packing of the "BaO_3" and "O_4" layers [12,15]. In a recent study of the Y–Ba–Fe–O system, we showed that effectively a cubic form was stable at room temperature, but with an excess of oxygen according to the formulation $YBaFe_4O_{7+\delta}$, due to oxidation in air [16]. In fact, it was shown that the stoichiometric $YBaFe_4O_{7.0}$ with a cubic symmetry was only stable at high temperature above ~573 K under reducing condition and was transformed to a tetragonal form below this temperature.

Bearing in mind, the possibility to generate new magnetic properties by distorting the lattice in "114" cobalt oxides, we have explored the structural, magnetic and transport properties of $YBaFe_4O_{7.0}$ in the range 300–4 K. Combining synchrotron X-ray (SXPD) and neutron (NPD) powder diffraction data, we show herein the existence of a new monoclinic form of $YBaFe_4O_{7.0}$

* Corresponding author.
E-mail address: vincent.caignaert@ensicaen.fr (V. Caignaert).

0022-4596/$ - see front matter © 2013 Elsevier Inc. All rights reserved.
http://dx.doi.org/10.1016/j.jssc.2013.06.002

below T_s~180 K, whose structure corresponds to a distortion of the tetragonal form, allowing a large decrease of the geometric frustration. For the first time in this series of "114" oxides, based on a distortion of the cubic close packing of the "BaO_7" framework a long range magnetic ordering is evidenced. The effect of this structural distortion on the magnetic and transport properties is also studied.

2. Experimental

2.1. Synthesis

Bearing in mind the extremely high sensitivity of the stoichiometric tetragonal $YBaFe_4O_{7.0}$ to oxidation in air at room temperature, special conditions of synthesis were carried out and care was taken to protect the samples from air oxidation during measurements. Two methods of synthesis of stoichiometric $YBaFe_4O_{7.0}$ were used, the previously described sealed tube method [16], and an original method under a flux of Ar/H_2. In the sealed tube method, stoichiometric mixtures of Y_2O_3 (99.9%, Alpha Aesar), $BaFe_2O_4$, Fe_2O_3 (99%, Merck) and Fe (99.5%, Alpha Aesar) are heated up to 1100 °C for 24 h. The sealed tube is then opened in an argon filled glove box in order to avoid any oxidation by air.

In the flux method, a precursor, obtained by citrate route, is equilibrated under an Ar/H_2 1% atmosphere humidified by bubbling in a saturator filled with distilled water cooled at 16 °C. The precursor is obtained by dissolving Y_2O_3 (99.9%, Alpha Aesar) and $BaCO_3$ (99.8%, Alpha Aesar) in a large excess of melted citric acid monohydrate (95.5%, Alpha Aesar) ($m_{Ac.citric}$~$20 \times m_{precursor}$) following the protocol previously described [17]. Fe(II) oxalate dihydrate (99%, Aldricht), used as an iron source, is firstly oxidized into the more soluble iron(III) oxalate by a drop by drop addition of concentrated hydrogen peroxide solution (35 wt% Alpha Aesar) in a suspension of iron(II) oxalate. When the reaction with H_2O_2 becomes less violent, the water volume is increased and the suspension is heated to boiling to finalize the dissolution and eliminate the peroxide excess. Finally, the dark brown oxalate solution is poured on the melted Ba–Y–citrate gel, the water is then evaporated, and the obtained gel is fired at 450 °C in air.

The so-obtained ashes do not exhibit any diffraction peak, confirming that the precursor is amorphous, and very good cation dispersion is expected due to the solution process. The ashes are pelletized in bars and placed in a corundum boat for the final annealing under humidified Ar/H_2 1%. The bars are heated (1 °C/min) up to 900 °C for 6 h, then to 1050 °C for 24 h, the furnace is then cooled as fast as possible to room temperature (~10 h). Since it is not possible to transfer the sample into the glove box without exposing it to air, we obtain the oxidized cubic $YBaFe_4O_{7+\delta}$ phase. The oxygen excess is removed by a 12 h annealing at 500 °C under Ar/H_2 5% atmosphere using a reduction cell design to fit in the glove box airlock. This technique allows the synthesis of large amounts of sample (~10 g) with good chemical homogeneity. Moreover, the smaller grain size of the citrate precursor allows a higher density of the ceramics (~90%) compared to the sealed tube method (~80%).

2.2. Elemental analysis and structural characterisation

Since most of the characterisation experiments cannot take place inside the glove box, the $YBaFe_4O_{7.0}$ tetragonal phase has to be mounted on holders that will protect it during transfer and/or analysis, as previously described [16].

The oxygen content was determined by cerimetric titration under argon atmosphere. The oxygen stoechiometry was found to be O7 within error of $\pm$ 0.02. The "$YBaFe_4$" cationic composition is checked by energy dispersive analysis (EDS) using an Oxford instrument analyser mounted on a FEI XL30 scanning electron microscope (SEM). In this latter case, no care is taken about the oxidation during the transfer.

The synchrotron X-ray powder diffraction (SXPD) experiments were performed on the X04SA beam line of the Swiss Light Source (SLS) of the Paul Scherrer Institute with a wavelength of λ=0.616 Å (20 keV) using the Mythen 1D detector that allow acquisition time of few seconds (preliminary measurements on the 11BM beam line of the Advanced Photon Source showed that the monoclinic phase is not stable under synchrotron X-ray irradiation (*to be presented elsewhere*). The powdered samples are loaded under controlled atmosphere in Ø=0.3 mm glass capillaries. The capillaries are corked with vacuum grease to be taken out of the glove box, and immediately flame sealed.

The neutron powder diffraction (NPD) experiments were performed on the Echidna high resolution diffractometer at the OPAL research reactor of the Australian Nuclear Science and Technology Organisation (ANSTO) with a wavelength of λ=2.44 Å. The samples are loaded, in the glove box, in a regular vanadium can and sealed by pressing an indium wire between the titanium flanges of the holder.

2.3. Magnetic measurements

The d.c. magnetization measurements were performed using a superconducting quantum interference device (SQUID) magnetometer with variable temperature cryostat (Quantum Design) with zero field cooled (ZFC), field cooled cooling (FCC) and field cooled warming (FCW) procedures in the range 300–10 K with an external field of 3000 Oe. The a.c. susceptibility was measured with a physical property measurement system (PPMS) from Quantum Design with a 10 Oe a.c. field in a 0 Oe static field at frequencies ranging from 80 Hz to 10 kHz. In both cases, the pelletized samples are introduced in a synthetic quartz tube (Ø=4 mm) filled with crushed quartz to hold the sample steady during the measurement. The tubes are corked with vacuum grease to be removed from the glove box and immediately flame sealed. The signal of a quartz tube filled with quartz powder is recorded to verify that the sample protection produces a diamagnetic perturbation that is essentially temperature independent and three orders of magnitude lower than the paramagnetic response of the sample at room temperature. The magnetic data are subsequently not corrected for such background signals.

2.4. Transport measurements

The resistivity measurements were performed with the transport option of the PPMS. A sintered bar (~1 cm length with a relative density of ~90%) is contacted with four, in line, platinum wires (Ø=40 μm) using platinum paste (Alpha Aesar), this first operation is performed in air. In order to dry the platinum ink and to reduce the sample to the $YBaFe_4O_{7.0}$ stoichiometry, the contacted bar is annealed at 500 °C in Ar/H_2 5% for 12 h and entered in the glove box without being exposed to air. The sample is then introduced in a small corundum container, covered with vacuum grease with the four wires lying outside of the container. The sample is then protected from oxidation during the transfer from the glove box to the cryostat of the PPMS. Due to the large size of the whole protection device, we have limited the heating and cooling rates to 1 K/min.

2.5. Mössbauer spectroscopy

Mössbauer spectra were collected between 295 K and 4 K in transmission mode using a conventional constant-acceleration spectrometer and a 25 mCi ^{57}Co source in a Rh matrix. The velocity scale was calibrated using α-Fe foil. Isomer shifts, IS, are given relative to this standard at room temperature. The absorbers were prepared inside the glove box by mixing the powder with vacuum grease (Rhodia) and spreading the mixture in a perspex holder. Low-temperature spectra were collected in a bath cryostat with the sample immersed in liquid He for measurements at 4 K and in He exchange gas for temperatures higher than 4 K. The spectra were fitted to Lorentzian lines using a non-linear least-squares method [18].

2.6. Calorimetry

Differential scanning calorimetry (DSC) analyses were performed using a DSC2920 from TA Instrument with speed of 10 K/min between 130 K and 300 K. The powdered sample is loaded in an airtight aluminium crucible, which is sealed by pressing the flange of the upper and lower part inside the glove box. The aluminium capsule is rapidly transferred from the glove box to the DSC apparatus.

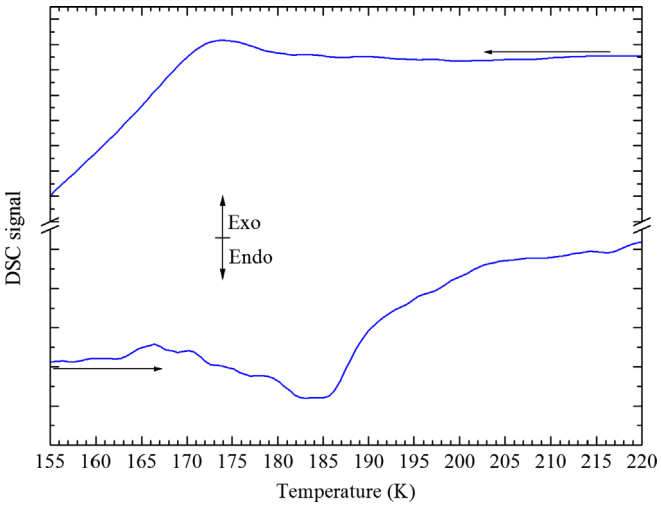

Fig. 2. Determination of the structural transition temperature by DSC.

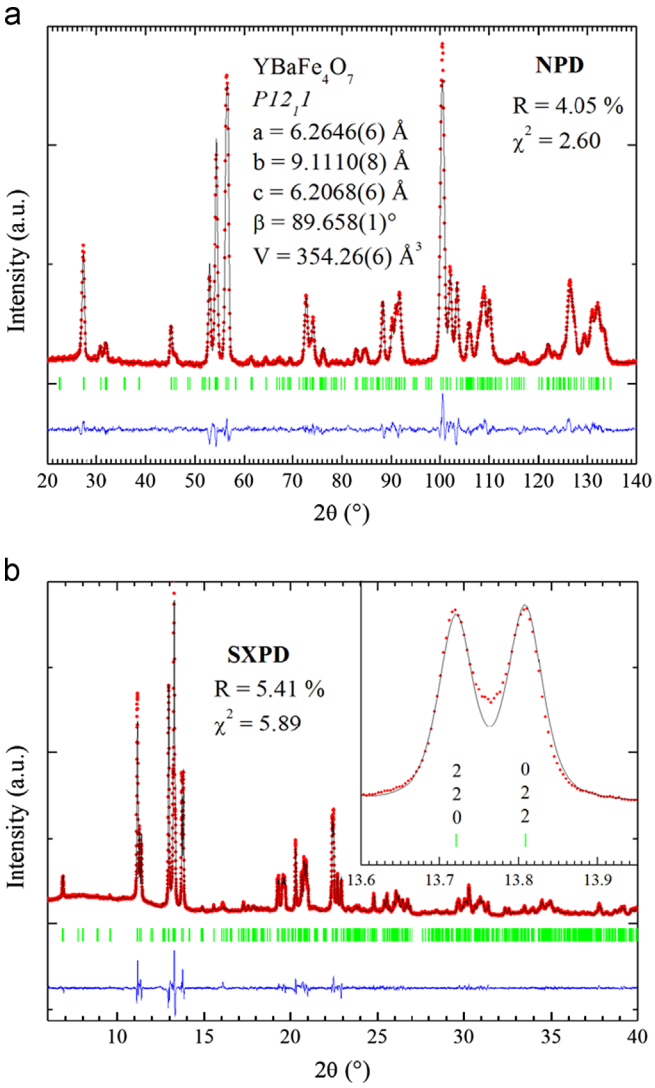

Fig. 1. Rietveld refinement of the (a) neutron and (b) synchrotron patterns of $YBaFe_4O_{7.0}$ at 110 K in the $P12_11$ space group. The inset shows asymmetric broadening due to scattering from domain walls.

3. Results and discussion

3.1. Nuclear structure of the monoclinic $YBaFe_4O_{7.0}$ oxide

The neutron and synchrotron patterns at 300 K confirm that the tetragonal $YBaFe_4O_{7.0}$ phase is obtained with good purity. The cell parameters, atomic positions, anisotropic thermal displacement parameters (ADPs) and microstructural effects are identical to our previous study [16]. As stated above, the observed tetragonal symmetry can be considered as a proof that no additional oxygen is inserted into the structure, *i.e.* $\delta=0$.

At 110 K the neutron and synchrotron patterns (Fig. 1) clearly show a new symmetry breaking structural transition. The patterns can be indexed in a monoclinic (M) cell ($a_M=6.2646(6)$ Å, $b_M=9.1110(8)$ Å, $c_M=6.2068(6)$ Å and $\beta=89.365(3)^\circ$) related to the parent $I\bar{4}$ tetragonal (T) cell as follow $a_M\sim a_T$, $b_M\sim c_T$, $c_M\sim a_T$ and $\beta\sim 90^\circ$. The transition temperature obtained from DSC (Fig. 2) shows a 10 K hysteresis between the maximum of the peak on cooling ($T=175$ K) and on warming ($T=185$ K), suggesting a first order transition.

The Rietveld refinement [19] of the structure was carried out simultaneously on the SXPD and NPD patterns, with the FullProf software [20] using the "mode crystallography" approach [21]. The low symmetry models and the corresponding distortion modes were calculated both from the 300 K tetragonal structure and from the 773 K cubic structure with the AMPLIMODES software [22]. We first tried to solve this new distortion in the $I121$ (unconventional centring of $C121$) space group which is the only monoclinic subgroup of $I\bar{4}$ with a k-index=1 [23]. This space group was rejected due to the refined values of the amplitudes of the two modes of the model. As a matter of fact, the amplitude of the GM1 mode, *i.e.* the mode that regroups all the atomic shifts allowed in the parent (tetragonal) symmetry, was found nearly ten times larger than the amplitude of the symmetry breaking mode GM2. Such a behaviour means that although the cell is undergoing a symmetry break, it would be stabilized only by atomic displacements allowed in the high symmetry structure.

Since there is no other monoclinic subgroup of $I\bar{4}$ with a zero propagation vector, superstructure reflexions were carefully searched out in the diffractograms. A family of low intensity peaks was spotted and successfully indexed with a $k=(1,1,1)$ propagation

vector on both SXPD and NPD patterns. Such a propagation vector means that the body centring of the cell is lost, implying a doubling of the primitive cell (k-index=2).

Two monoclinic space groups are subgroups of $I\bar{4}$ with a k-index=2: $P12_11$ and $P121$ [23]. The refinements were carried out in the two groups, but $P12_11$ was selected because all the 0 k 0 reflexions with $k=2n$ are absent and atomic positions of the $P121$ model were keeping the symmetry relations of the 2_1 axis. Moreover, $P12_11$ is an isotropy subgroup of both $I\bar{4}$ and $F\bar{4}3m$ space groups of the high temperature structures, contrary to $P121$.

Table 1
Details of the Rietveld refinement of the synchrotron and neutron diffractograms of the monoclinic phase of $YBaFe_4O_{7.0}$ at 110 K.

	SXPD	NPD
Space group	$P12_11$	
Cell parameters (Å)	a=6.2646(6) b=9.1110(8) c=6.2068(6)	
Monoclinic angle (°)	β=89.365(3)	
Wavelength (Å)	0.616610	2.440601
Step (°)	0.00393	0.05
χ^2	5.89	2.60
R_{Bragg} (%)	5.41	4.05

Atom	Wyck.	x	y	Z	Biso (Å^2)
Y	2a	0.750(3)	0.75	0.254(3)	0.15(2)
Ba	2a	0.736(2)	0.500(1)	0.753(2)	0.77(3)
Fe1	2a	0.735(3)	0.130(2)	0.004(3)	0.55(2)
Fe2	2a	0.491(3)	0.378(2)	0.270(3)	0.68(3)
Fe3	2a	0.981(3)	0.369(2)	0.232(3)	1.2(1)
Fe4	2a	0.774(3)	0.140(2)	0.469(3)	0.68(3)
O1	2a	0.749(6)	0.500(2)	0.235(6)	2.4(3)
O2	2a	0.735(6)	0.000(2)	0.249(6)	0.32(2)
O3	2a	0.536(6)	0.264(5)	0.525(6)	0.13(2)
O4	2a	0.947(6)	0.284(5)	0.937(6)	0.34(2)
O5	2a	0.063(6)	0.214(4)	0.449(6)	0.59(4)
O6	2a	0.470(6)	0.234(4)	0.043(6)	0.90(6)
O7	2a	0.750(9)	0.007(5)	0.750(9)	1.2(1)

The atomic positions obtained from the combined Rietveld refinement of the SXPD and NPD patterns of $YBaFe_4O_{7.0}$ at 110 K, in the $P12_11$ space group, are listed in Table 1. The iron atoms, located on a unique crystallographic site in the tetragonal cell, are split in four non-equivalent positions in the monoclinic cell, allowing the differentiation of their coordination sphere.

The χ^2 factors of those refinements are rather high, especially in the case of the synchrotron pattern. Conversely, the R_{Bragg} values are low, meaning that the high values of χ^2 are due to inefficient modelling of the profile rather than poor fit of the diffracted intensities. Indeed the general aspect of the refinement is correct (Fig. 1) but a closer look at the split reflexions (inset Fig. 1b) clearly evidences microstructural phenomena. Just like in the patterns of the 300 K tetragonal phase [16], the twinning domains created because of the loss of rotational symmetry elements give rise to *hkl* dependent asymmetric profile. These issues are not addressable in the FullProf software. Moreover, the large number of atomic parameters and the low symmetry of the $P12_11$ space group make it impossible to work with anisotropic atomic displacement

Table 2
Mode decomposition of the monoclinic structure of $YBaFe_4O_{7.0}$ at 110 K.

k-Vector	Mode	Direction	Isotropy subgroup	Dimension	Amplitude (Å)
(a) Parent structure: $YBaFe_4O_{7.0}$ at 500 °C ($F\bar{4}3m$)					
(0,0,0)	GM1	(a)	$F\bar{4}3m$	2	0.26(2)
(0,0,0)	GM3	(a,b)	$F222$	4	0
(0,0,0)	GM4	(a,0,0)	$Imm2$	8	0.18(3)
(0,0,0)	GM5	(a,0,0)	$I\bar{4}$	3	1.37(2)
(0,1,0)	X5	(b, − b,a, a,0,0)	$P12_11$	22	0.56(4)
(b) Parent structure: $YBaFe_4O_{7.0}$ at 25 °C ($I\bar{4}$)					
(0,0,0)	GM1	(a)	$I\bar{4}$	7	0.15(2)
(0,0,0)	GM2	(a)	$C2$	10	0.18(3)
(1,1,1)	M3M4	(a,b)	$P12_11$	22	0.56(4)

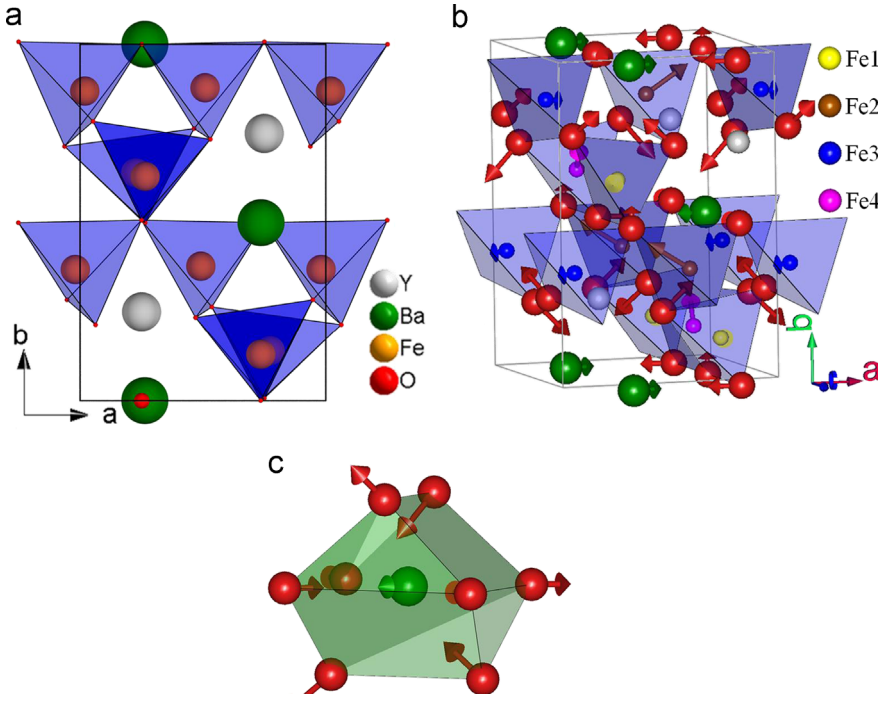

Fig. 3. Representation of (a) the monoclinic phase of $YBaFe_4O_{7.0}$ at 110 K, (b) of the atomic shifts stabilizing the monoclinic structure with respect to the tetragonal or cubic phase (sum of GM2+M3M4 or GM4+X5, respectively) and (c) close-up on the [BaO_8] deformation.

Table 3
Comparison of the bonds length between the 300 K tetragonal and the 110 K monoclinic structures of $YBaFe_4O_{7.0}$.

	Tetragonal 300 K	Monoclinic 110 K
Y–O	2.26(1) (× 4)–2.25(1) (× 2) Å	2.22(3)–2.25(3) (× 2) Å 2.28(1) (× 2)–2.31(3) Å
Average	**2.26 Å**	**2.27 Å**
Ba–O	2.79(1) (× 4) Å	2.63(3)–2.64(3)–2.79(3)–2.87(3) Å 2.95(3)–2.99(3)–3.21(3)–3.31(3) Å
Average	3.133(2) (× 4) Å	**2.92 Å**
	2.96 Å	
Fe1–O	1.95(1)–1.94(1) (× 2)–2.012(6) Å	1.93(3) (× 3)–1.97(3) Å
Average	**1.96 Å**	**1.94 Å**
Fe2–O	–	1.92(3) (× 2)–1.93(3)–1.97(3) Å
Average		**1.94 Å**
Fe3–O	–	1.88(3)–2.00(3)–2.02(3)–2.11(3) Å
Average		**2.00 Å**
Fe4–O	–	1.88(3)–1.90(3)–1.94(3)–2.13(3) Å
Average		**1.96 Å**
Fe–Fe in [Fe_4]	3.059(8) (× 2) Å	2.86(2)–2.90(2) Å
Average	3.022(2) (× 4) Å	3.02(2)–3.07(2)–3.07(2)–3.19(2) Å
	3.034 Å	**3.02 Å**
Fe–Fe in [Fe_4O]	3.260(8) (× 2) Å	3.19(2)–3.21(2) Å 3.32(2)–3.32(2)–3.30(2)–3.47(2) Å
Average	3.300(8) (× 4) Å	**3.30 Å**
	3.287 Å	

parameters (ADP), leading to a less efficient modelling of the oxygen position, especially those of the barium coordination sphere.

The values of the parameters of the monoclinic cell show that the distortion consists mostly in the contraction (-1%) of the c_M parameter and in the decrease (-0.34°) of the β angle. The deformation of the cell is not very significant, so only small atomic shifts are expected to stabilize the structure. Therefore the monoclinic structure is close to the tetragonal one (Fig. 3) and the modifications induced by this structural transition are significantly smaller than those due to by the cubic to tetragonal transition.

The monoclinic structure can be described using either the high temperature (773 K) cubic ($F\bar{4}3m$) model (Table 2a) or the room temperature tetragonal ($I\bar{4}$) model (Table 2b) as the parent phase. The two descriptions are completely equivalent, but they help to emphasize that the monoclinic transition comes in addition of the tetragonal distortion. The description based on the cubic model shows that the amplitude of the primary mode GM5 of the tetragonal distortion has a much larger amplitude (1.37(2) Å) than the modes GM4 and X5 (0.18(3) Å and 0.56(4) Å, respectively) introduced by the symmetry break of the monoclinic transition. It also points out that the degrees of freedom with the $F222$ isotropy space group corresponding to the GM3 mode are not used to stabilize the structure, allowing to refine the structure with four less atomic parameters than with a classical approach.

On the other hand, the tetragonal based description relates the differences between the room temperature structure and the monoclinic structure. The greater importance of the modes introduced by the symmetry break (GM2 and M3M4) compared to the mode GM1 that possesses the $I\bar{4}$ isotropy space group is more straightforward in this description. It is then easier to check that the monoclinic structure is stabilized by atomic shifts that are not allowed in the parent phase.

Note that the primary mode M3M4 of the tetragonal to monoclinic distortion is not sufficient to describe the low temperature structure. Indeed, the secondary mode GM2 has a non-zero amplitude that requires this structural transition to be of first order. As a consequence, there is no difference, within the experimental resolution, between atomic positions of $YBaFe_4O_{7.0}$ at 110 K and at 4 K, even the cell parameters remain nearly constant with a cell volume difference less than 0.01%.

The atomic shifts stabilizing the monoclinic distortion are represented on Fig. 3b. The atomic positions in this representation are those generated by the modes compliant with the $I\bar{4}$ space group, *i.e.* atomic shifts that are allowed in the tetragonal structure. The arrows (Fig. 3b) show the atomic shifts resulting from the tetragonal ($I\bar{4}$) to monoclinic ($P12_11$) symmetry break, *i.e.* the combination of GM4 and X5 in the cubic based description or the combination of GM2 and M3M4 in the tetragonal based description. All the atoms of the cell, except yttrium, are shifted, which makes the interpretation of the transition complex.

The barium underbonding, which was found to be the reason of structural transitions in stoichiometric 114 Co-based [4] as well as Fe-based [16] oxides, seems to play also an important role in this transition. All the arrows modelling the shifts of the oxygen atoms are pointing in the direction of a Ba site. Barium atoms are also shifting along the [1 0 0] direction toward an oxygen atom. As a consequence, the bond valence sum calculations performed for the 110 K-monoclinic structure gives a value of BVS(Ba)=1.63, to be compared to the value of 1.43 found in the tetragonal structure at 300 K. The interatomic distances (Table 3) show that the YO_6 octahedra are only slightly more distorted than in the tetragonal form. It is not the case of the FeO_4 tetrahedra. Two FeO_4 tetrahedra, Fe1 and Fe2, are not significantly distorted, like in the tetragonal structure, whereas the two other tetrahedra, Fe3 and Fe4, are much more distorted, with Fe–O distances ranging from 1.88(3) Å to 2.13(3) Å. The evolution of the coordination sphere of the Ba atoms through the monoclinic distortion (Fig. 3c and Table 3) shows that two of the short Ba–O bonds are shrinking from 2.79(1) Å at 300 K to 2.63(3) Å and 2.64(3) Å at 110 K whereas the others two are stretching from 2.79(1) Å at 300 K to 2.87(3) Å or remain constant (2.79(3) Å) despite the thermal contraction. The same kind of behavior is seen on the four longer bonds that form the equatorial square plane in the BaO_8 coordination polyhedra. Thus, it must be emphasized that during this tetragonal to monoclinic transition, two oxygen atoms strongly linked to barium are displaced toward iron, in spite of the large underbonding of barium. Interestingly, considering the Fe–O–Ba bonds, the Fe2 site is the only one for which two corresponding Ba–O bonds become less strong after the tetragonal to monoclinic distortion.

3.2. Magnetic structure of the monoclinic $YBaFe_4O_{7.0}$

The NPD patterns show the presence of additional reflexions for temperatures lower than 100 K (Fig. 4a). These reflexions are not present on the SXPD patterns, confirming their magnetic origin. The superimposition of the NPD patterns at 85 K and 4 K

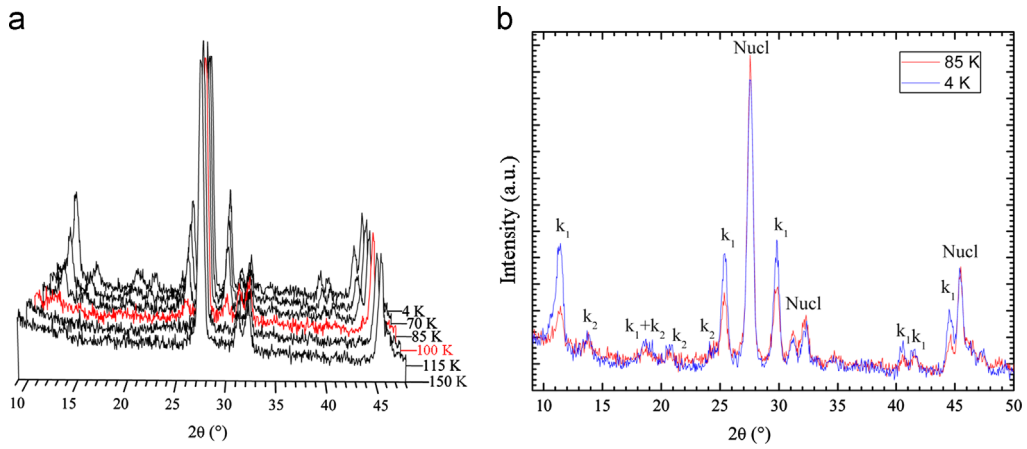

Fig. 4. Evolution of the NPD pattern with temperature.

clearly shows that there are in fact two families of magnetic reflections with different temperature dependence (Fig. 4b). The most intense reflexions are indexed with the propagation vector $k_1=(0,0,½)$ with reference to the monoclinic cell. The corresponding magnetic intensity increases gradually as the temperature is lowered, suggesting a second order transition. In contrast, the second set of reflections is much weaker. The latter exhibit an incommensurate propagation vector $k_2=(0.344(1),0,½)$ which does not evolve with temperature.

Since the intensity of the reflexions indexed with k_2 are very weak, it was not possible to solve the associated magnetic structure, and those intensities fitted using a Le Bail protocol [24]. Therefore only the resolution of the magnetic structure corresponding to k_1, at 4 K where the maximum magnetic intensity is recorded, has been established. Nevertheless, it is worth pointing out that the value of k_2 is consistent with a tripling of the k_1 magnetic cell, suggesting that a small volume fraction of the sample might exhibit a more complex magnetic arrangement, eventually due to a slight oxygen stoichiometry inhomogeneity.

The propagation vector $k_1=(0,0,½)$, is a special point (B) of the first Brillouin zone and is equivalent to $-k_1$. The two symmetry elements of the $P12_11$ space group $(1, 2_1)$ are compatible with k_1. The magnetic representation of each iron site located in a general 2a (x,y,z) position is decomposed into six basis vectors (ψ_1 to ψ_6) based on two irreducible representations of order 1, $\Gamma_{Mag}=3\Gamma_1\oplus3\Gamma_2$. According to the Γ_1 representations, two atoms related by symmetry operation, A and B, have the same magnetization coordinate along x and z ($m_{xA}=m_{xB}$ and $m_{zA}=m_{zB}$) but reverse coordinates along y ($m_{yA}=-m_{yB}$). The Γ_2 representation possesses exactly the opposite relations $m_{xA}=-m_{xB}$, $m_{yA}=m_{yB}$, $m_{zA}=-m_{zB}$ (Table 4).

The magnetic transition associated with the k_1 propagation vector being a second order one, only one irreducible representation should be sufficient to describe the magnetic structure. Both representations were then separately tested, using the reverse Monte-Carlo (RMC) procedure within the FullProf software. The models satisfying the symmetry relations fixed by the Γ_1 irreducible representation produce a much better agreement than the models based on Γ_2.

In all the models obtained through RMC simulations based on Γ_1, the iron sites Fe1, Fe2 and Fe3 are carrying a magnetic moment with a coordinate along the monoclinic **b** axis that is much larger than the two others. This fact allows us to limit the number of parameters used in the final Rietveld refinement; the moments of Fe1 to Fe3 are constrained along **b**, whereas the three coordinates of the moment on Fe4 are refined. By doing so, we obtain stable refinements of the magnetic neutron pattern (Fig. 5) with agreement factors as low as $R_{mag}(k_1)=4.39\%$ and $\chi^2=1.81$.

Table 4
Description of the magnetic representation of the iron sites.

Irreducible representation	Basis vector	Atom A			Atom B		
		m_x	m_y	m_z	m_x	m_y	m_z
Γ_1	ψ_1	1	0	0	1	0	0
	ψ_2	0	1	0	0	−1	0
	ψ_3	0	0	1	0	0	1
Γ_2	ψ_4	1	0	0	−1	0	0
	ψ_5	0	1	0	0	1	0
	ψ_6	0	0	1	0	0	−1

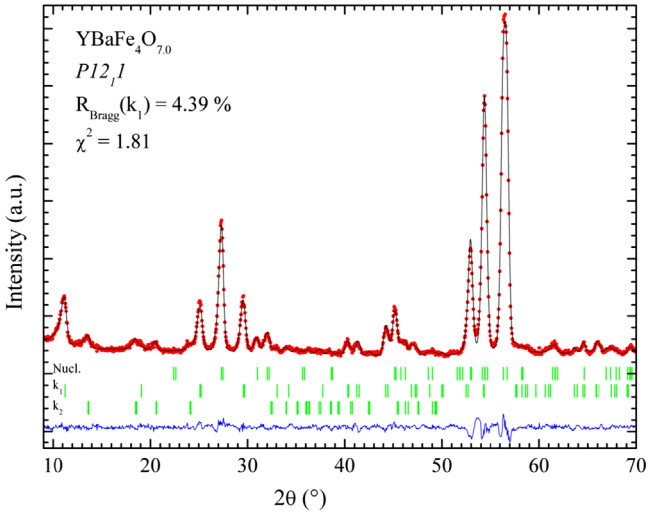

Fig. 5. Rietveld refinement of the magnetic structure of $YBaFe_4O_{7.0}$ at 4 K (intensities associated with k_2 are accounted with Le Bail fit procedure).

The magnetic structure (Table 5) refined with the previously mentioned restrictions clearly shows a larger moment on the Fe2 site than for the three other sites (Fe1, Fe3 and Fe4), which are close to each other. The obtained values of the magnetic moments of 3.1 μ_B for Fe2 and of 2.4 to 2.6 μ_B for Fe1, Fe3 and Fe4 are significantly lower than the expected values for iron in high spin configuration, as imposed by its tetrahedral coordination, *i.e.* $M\sim5\ \mu_B$ for Fe^{3+} and $M\sim4\ \mu_B$ for Fe^{2+}. Nevertheless, the significantly larger value observed for Fe2, suggests that the Fe2 site should be preferentially occupied by Fe^{3+}, whereas Fe^{2+} should sit on the other sites Fe1, Fe3, Fe4. Such lower values of the magnetic moments, compared to the theoretical ones can easily be

explained by the high tendency of the tetrahedral iron sublattice to exhibit magnetic frustration. Indeed, in the cubic form, the $[Fe_4]_\infty$ sublattice built up of regular Fe_4 tetrahedra similar to pyrochlores involves a strong 3D geometric frustration. Despite the large distortion of the $[Fe_4]_\infty$ sublattice, it is most probable that the competition between magnetic ordering and geometrical frustration remains high in the monoclinic structure. An important part of the spins are then still fluctuating below the magnetic ordering temperature. This oscillating fraction decreases with temperature, explaining the constant increase of the diffracted magnetic intensity. Thus, due to that phenomenon the existence of charge ordering cannot be unambiguously proven based on NPD data.

Table 5
Directions and magnitudes of the magnetic moments of $YBaFe_4O_{7.0}$ at 4 K.

Site	m_x	m_y	m_z	m_{tot} (μ_B)
Fe1	0	2.63(16)	0	2.63
Fe2	0	3.11(16)	0	3.11
Fe3	0	−2.58(11)	0	2.58
Fe4	1.20(15)	1.66(16)	−1.24(32)	2.38

The number of possible exchange pathways in this structure is very large (Fig. 6), each iron atom is surrounded by six crystallographically independent iron sites, giving rise to six direct exchange pathways, with Fe–Fe distances ranging from 2.86 Å to 3.46 Å. In addition, all the iron atoms are connected by pairs through a bridging oxygen site, opening possible superexchange pathways. Two different configurations are present: (i) iron atoms in Fe_4O tetrahedra are bridged by the central oxygen atom, with Fe–O–Fe bond angles ranging from 105.65° to 111.90° (ii) iron atom in Fe_4 tetrahedra are linked by pairs by one of the six oxygen atoms of the LnO_6 octahedra, with Fe–O–Fe bond angle ranging from 92.54° to 111.36°.

Thus, considering the $[Fe_4]_\infty$ sublattice, built up of corner-sharing Fe_4 and Fe_4O tetrahedra (Fig. 6a), as well as the Fe_4O_7 framework (Fig. 6c) it appears clearly that most of the Fe–O–Fe angles deviate strongly from 90° to 180°. Moreover, Fe–Fe distances are significantly short, especially within the Fe_4 tetrahedra; the topology of the Fe_4O_7 framework implies an axial overlap of the t_2 orbitals of the metallic centers in the Fe_4 and Fe_4O

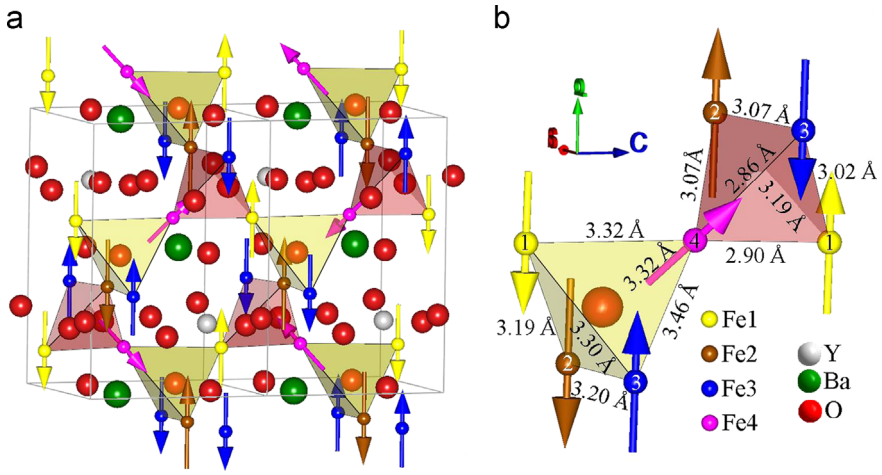

Fig. 6. Visualization of magnetic structure of $YBaFe_4O_{7.0}$ along [1 0 0] at 4 K (a) full magnetic cell and (b) detailed view of the $[Fe_4]$ and $[Fe_4O]$ tetrahedra.

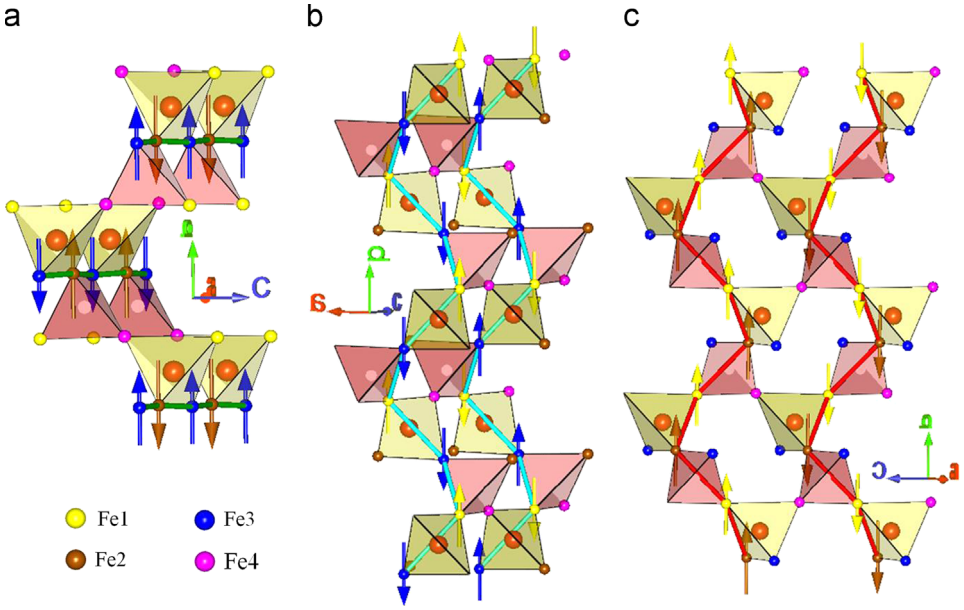

Fig. 7. Representation of the different chains (a) antiferromagnetic Fe2–Fe3, (b) antiferromagnetic helicoidal Fe1–Fe3 and (c) ferromagnetic helicoidal Fe1–Fe2.

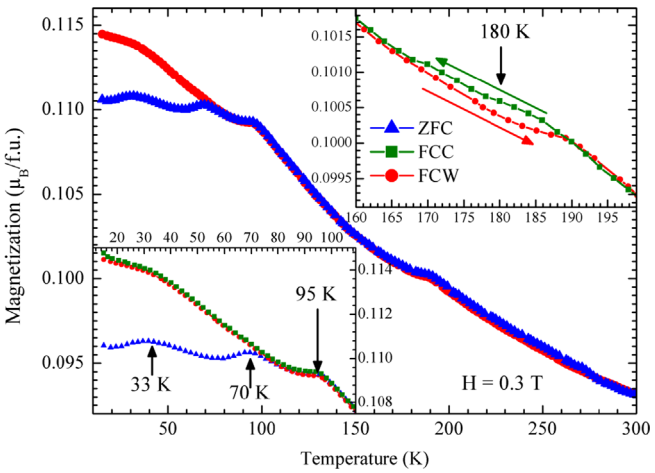

Fig. 8. Magnetization curves of $YBaFe_4O_{7.0}$ *vs.* temperature recorded according to the zero field cooled (ZFC), field cooled cooling (FCC) and field cooled (FCW) procedure.

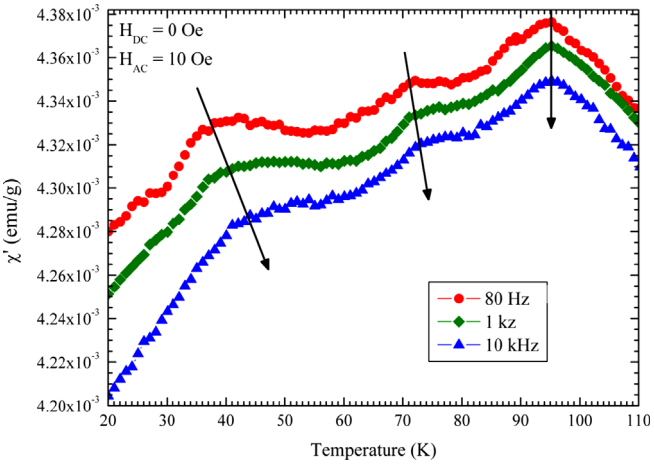

Fig. 9. Real part of the a.c. magnetic susceptibility of $YBaFe_4O_{7.0}$.

tetrahedra. This strongly suggests that the direct exchange magnetic interactions due to the overlap of the cations orbitals, as described by Goodenough [25], prevail largely over the superexchange interactions. Such a direct exchange formalism was indeed considered for explaining the magnetic properties of the spinels ACr_2X_4 [26–28] where the strength of the antiferromagnetic interactions due to the overlap of the t_{2g} orbitals was found to be more important than superexchange for Cr–Cr distances ranging from 2.94 Å to 3.52 Å. Note however that, differently from the spinel structure, the tetrahedral coordination of iron in the present structure implies that the energy level of the t_2 orbitals is higher than the energy level of the e orbitals. Therefore, strong antiferromagnetic interactions are expected between two cations with $n \leq 7$ electrons in their d shells (instead of $n \leq 5$ in octahedral coordination).

This means that antiferromagnetic interactions are expected between all the iron sites, Fe^{2+}–Fe^{2+} as well as Fe^{2+}–Fe^{3+}, resulting in magnetic frustration due to the topology of the $[Fe_4]_\infty$ framework. This is indeed observed for the spins of Fe1, Fe2 and Fe3 which are all collinear, *i.e.* parallel to $\vec{b}$ (Fig. 6b). Fe2 and Fe3, as well as Fe3 and Fe1 are antiferromagnetically coupled in both Fe_4 and Fe_4O tetrahedra. Those two couplings generate two antiferromagnetic chains, one Fe3–Fe2 along $\vec{a}$ (Fig. 7a) and a helical chain Fe1–Fe3 spiraling along $\vec{b}$ (Fig. 7b). Conversely, Fe1 and Fe2 are ferromagnetically coupled in both Fe_4 and Fe_4O tetrahedra, creating ferromagnetic helical chains along $\vec{b}$ (Fig. 7c). It is interesting to note that in both Fe_4 and Fe_4O tetrahedra, Fe1–Fe2 distances are very similar, as well as Fe–O distances (1.92–1.93 Å) and Fe1–O–Fe2 angles (111.36° and 111.90°). This suggests that this ferromagnetic coupling is not simply due to the fact that Fe1–Fe2 is the longest distance in the Fe_4 tetrahedra, *i.e.* the weakest antiferromagic interaction. This peculiar geometry, found all along the ferromagnetic chain, might favor ferromagnetic exchange at the expense of the direct antiferromagnetic exchange, lifting an important part of the magnetic frustration of the structure.

The spin of Fe4 cannot be collinear with those of Fe1, Fe2 and Fe3 since this would generate a too high magnetic frustration due to the short distance (< 2.90 Å) ferromagnetic interaction that would be established within either Fe1 or Fe3. As a consequence, it is directed along the two edges of Fe_4 and Fe_4O tetrahedra (see line Fe2–Fe4–Fe3 Fig. 6b), reducing strongly its magnetic moment along $\vec{b}$ to $m_y \sim 1.66\ \mu_B$ (Table 5). The orientation of the spin of Fe4 is then probably the result of a competition between weaker magnetic interactions.

It is noteworthy to remind here that the nuclear structure does not evolve in a significant way between 110 K and 4 K, in spite of the ordering of the magnetic moments. This means that the interactions between the spins do not produce any modification of the nuclear framework. This, as well as the large difference between the structural and magnetic transition temperatures, points out that the long range magnetic order is a consequence of the structural distortion and not a cause.

3.3. *Magnetic properties.*

The dc magnetization curves *vs.* temperature of $YBaFe_4O_{7.0}$ exhibit a complex magnetic behaviour (Fig. 8). Similarly to $YBaCo_4O_7$ [2,29], the structural transition of $YBaFe_4O_{7.0}$ has a clear signature in the magnetization curves due to the small hysteresis spotted around 180 K between the curves registered while warming the sample (ZFC, FCW) and the curve registered while cooling the sample (FCC) (upper right inset Fig. 8).

The signal at 95 K corresponds to the appearance of the magnetic reflections observed on the NPD patterns and can then be attributed to the transition from the paramagnetic state to the antiferromagnetic state. Unlike the structural transition at 180 K, this magnetic transition does not exhibit any hysteresis between the ZFC, FCW and the FCC curves, supporting the fact that it is a second order transition. Two other magnetic transitions are present on the magnetic curves, at 70 K and 33 K, respectively. In order to understand this behaviour, ac-susceptibility measurements were performed.

The $\chi'(T)$ curves registered at different frequencies of the magnetic field of 80 Hz, 1 kHz and 10 kHz (Fig. 9) show that the transition at 95 K is frequency independent in agreement with the paramagnetic to antiferromagnetic transition observed from NPD. The peak positions corresponding to the two other transitions at ~40 K and ~70 K depend on the frequency, suggesting the existence of short range ordering and/or magnetic frustration leading to a glassy state. This behavior is in agreement with the magnetic moment values of iron obtained from NPD data, which strongly suggest a competition between magnetic frustration and antiferromagnetic ordering in this structure, due to the great ability of the 3D $[Fe_4]_\infty$ lattice to geometric frustration. Moreover, oxygen traces may also be present in those samples due to the extremely high sensitivity of $YBaFe_4O_{7.0}$ to oxidation. Thus, $YBaFe_4O_{7+\delta}$ clusters with a spin glass behavior [12], might be formed during the encapsulation of the sample. Nevertheless, the T_g value of the air exposed samples ~50 K, is very different from the values observed here, strongly suggesting that the oxidation, if any, is very weak and takes place locally leading to a different local magnetic frustration.

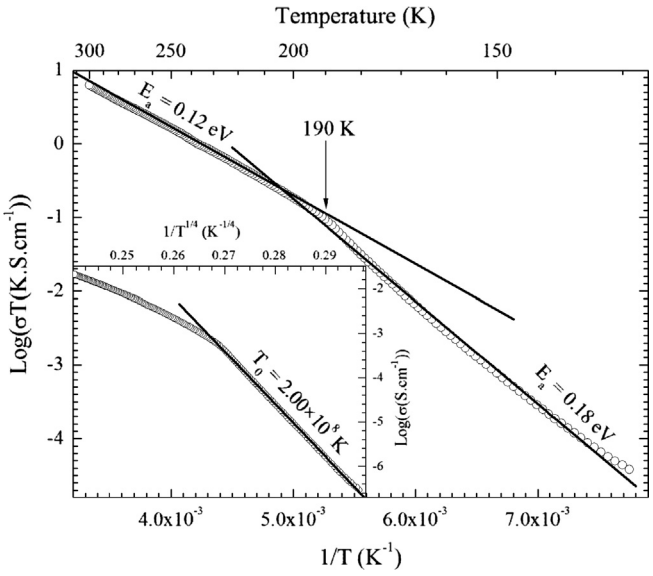

Fig. 10. Resistivity of $YBaFe_4O_{7.0}$ fitted with a thermally activated hopping model $\sigma = ((\sigma_0/T)\exp(-E_a/kT))$. Inset: Low temperature, monoclinic, domain fitted with a 3-D variable range hopping model $\sigma = \sigma_0 \times \exp(-T_0/T)^{1/4}$.

3.4. Transport properties

The evolution of the conductivity *vs.* temperature of $YBaFe_4O_{7.0}$ (Fig. 10) shows a semi-conducting behaviour in the whole range of studied temperatures (300–130 K). The conductivity values are small, ~20 mS/cm at room temperature, *i.e.* nearly two orders of magnitude lower than those in the "114" cobaltites $LnBaCo_4O_7$ [3,29–34]. Since the relative density of the sintered sample was approximately 90%, the total conductivity may be improved by a better densification of the material. Because of the high resistivity of the sample the temperature range was limited to 130 K; the influence of the magnetic order could not be studied.

The structural transition from the tetragonal to monoclinic structure is also clearly evidenced in the resistivity measurements by a slope break at 190 K. For temperatures higher than 190 K, Log(σT) follows a linear evolution *vs.* temperature, corresponding to a thermally activated hopping model

$$\sigma = \frac{\sigma_0}{T}\exp\left(\frac{-E_a}{kT}\right)$$

with a small activation energy of $E_a = 0.12$ eV. This behavior and the value of activation energy are compatible with a small-polaron mechanism frequently observed in mixed valent oxides.

For temperatures lower than 190 K, the conductivity of the monoclinic sample decreases much faster with the temperature than at higher temperature. Moreover, the poor fit obtained with the thermally activated conductivity model also indicates a change in the transport mechanism. A much more consistent fit was obtained by applying a 3D variable range hopping (VRH) model $\sigma = \sigma_0 \times \exp(-T_0/T)^{1/4}$ (inset Fig. 10) with an extracted Mott temperature of $T_0 = 2.00 \times 10^8$ K.

The stronger dependence of the conductivity with temperature and the change of mechanism are both consistent with localisation of the electrons. The electronic system switches at 190 K from a delocalized state, where all the electrons hops are equivalent, to a localized electronic system where the electrons are fixed on a specific position. The number of possible configurations is then much larger, especially due to the monoclinic distortion which multiplies the number of independent iron sites by four. The VRH model is more suitable to explain such a disordered system. Note that, even if this change is characteristic of the charge localisation, it does not imply that this localization is necessarily ordered.

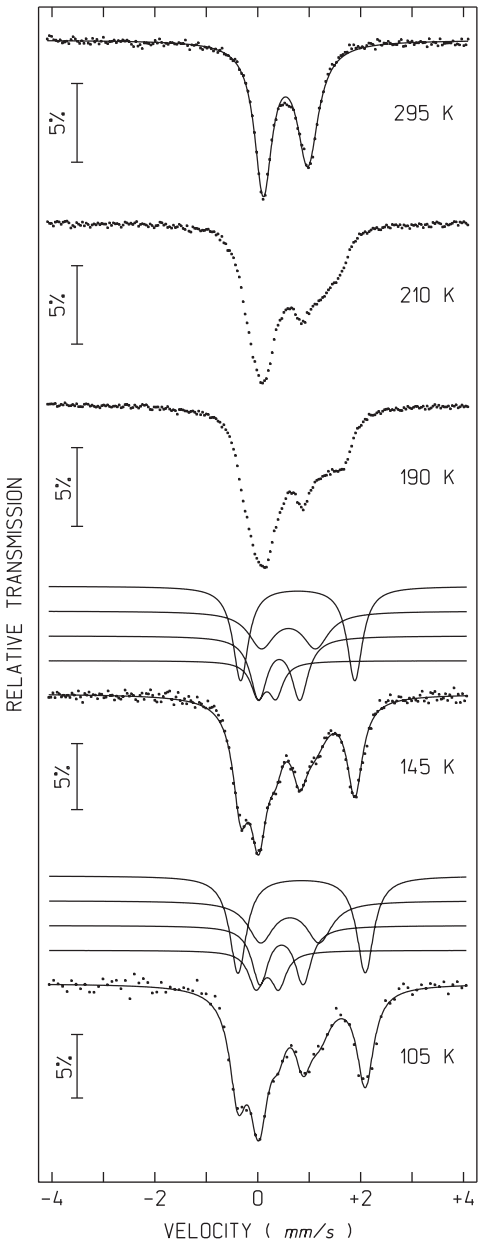

Fig. 11. Mössbauer spectra of $YBaFe_4O_{7.0}$ at different temperatures in the paramagnetic state.

3.5. Mössbauer spectroscopy

At room temperature an asymmetric doublet is observed. An analysis with two symmetric doublets leads to IS = 0.39 for one of them and 0.57 mm/s for the second one. At room temperature 0.39 mm/s is too high for Fe^{3+} in tetrahedral coordination in oxides [18,35] and 0.57 mm/s too low for Fe^{2+} [36]. As already reported [16] the refinement with one doublet converges to isomer shift IS = 0.64 mm/s relative to Fe metal at 295 K, quadrupole splitting QS = 0.86 mm/s. IS = 0.64 mm/s is intermediate between the IS range of values typical for Fe^{3+} and Fe^{2+}. The asymmetry of the spectrum may be related to the fact that there is neither an average oxidation state $Fe^{2.25+}$ nor definite Fe^{2+} and Fe^{3+} states. This situation is similar to that found for $RBaFe_2O_{5-\delta}$ double perovskites [37–39]. In these compounds intermediate

Table 6
Parameters estimated from the Mössbauer spectra of $YBaFe_4O_{7.0}$ taken at different temperatures.

	IS (mm/s)	**QS** (mm/s)	**I**	**Fe oxidation state**
295 K				
	0.64	0.86	100	$Fe^{2.25+}$
145 K				
	0.28	0.39	12%	Fe^{3+}
	0.54	0.80	27%	$Fe^{2.25+\varepsilon}$
	0.74	1.04	24%	$Fe^{2.25-\varepsilon}$
	0.89	2.22	37%	Fe^{2+}
105 K				
	0.30	0.41	12%	Fe^{3+}
	0.58	0.84	27%	$Fe^{2.25+\varepsilon}$
	0.74	1.14	24%	$Fe^{2.25-\varepsilon}$
	0.97	2.47	37%	Fe^{2+}

IS (mm/s) isomer shift relative to metallic α-Fe at 295 K; QS (mm/s) quadrupole splitting estimated from quadrupole doublets; I relative area. Estimated errors are ± 0.02 mm/s for IS, QS, and $\pm 2\%$ for I.

valence states, $Fe^{2.5+\delta}$ and $Fe^{2.5-\delta}$ $(0<\delta<0.5)$, were observed within a temperature range intermediate between fully mixed-valence and charge-ordered states. In the present $YBaFe_4O_7$ case we would rather have intermediate $Fe^{2.25+\varepsilon}$ and $Fe^{2.25-\varepsilon}$ charge states (with $0<\varepsilon<0.25$) since in this oxide the average oxidation state of the iron cations is +2.25. The inhomogeneous delocalized electronic system among the Fe cations may be related to hybridized Fe^{3+}–O–$Ba^{+}\leftrightarrow Fe^{2+}$–O–$Ba^{2+}\leftrightarrow Fe^{3+}$–O–$Ba^{2+}$ bonds [16].

The gradual evolution of the shape of the spectra in the range 295–190 K (Fig. 11), suggesting a slowing down of the thermally activated electron exchange rate, supports this assumption. The broadening of the absorption lines seems related to dynamical effects resulting from electron exchange rates with a characteristic frequency $\tau_{CT}\sim 10^8\ s^{-1}$, of the same order of magnitude of the reciprocal of the Mössbauer effect time-window.

Below the structural transition at 180 K there is a clear narrowing of the absorption peaks. The spectra at 145 K and 105 K may be fitted by four quadrupole doublets (Table 6 and Fig. 11). The doublet with the lowest IS (0.28 mm/s and 0.30 mm/s at 145 K and 105 K, respectively) may be assigned to Fe^{3+} in tetrahedral coordination [18,35] while the highest IS (0.89 mm/s and 0.97 mm/s at 145 K and 105 K, respectively) are already within the range of Fe^{2+} isomer shift values. The remaining doublets with IS = 0.54–0.58 mm/s and 0.74 mm/s, in-between those of Fe^{3+} and Fe^{2+}, suggest that at this stage there still are intermediate charge states $Fe^{2.25+\varepsilon}$ and $Fe^{2.25-\varepsilon}$, respectively. The ratio of the estimated relative areas for the Fe^{3+} and Fe^{2+} doublets, Fe^{3+}:Fe^{2+} is approximately 1:3, in agreement with the ideal $YBaFe_4O_{7.0}$ stoichiometry and confirming that the average oxidation state of the remaining Fe cations is +2.25.

Thus, Mössbauer spectroscopy reveals that the change in the conduction mechanism, from a thermally activated hopping model to a VRH model, at the structural transition can be related to a change in the electronic delocalization. The differentiation of the iron sites, due to the monoclinic transition, induces preferential, but not exclusive, hopping directions. The different probabilities of electron transition result in a statistical distribution of at least four different oxidation states in the monoclinic structure of $YBaFe_4O_{7.0}$. This is a conclusive proof that only a partial charge ordering is achieved through the monoclinic distortion.

Below 90 K magnetic interactions become apparent in the spectra. This sudden drop in the relaxation time of the Fe magnetic moments, μ_{Fe}, reveals the establishment of long-range magnetic correlations as confirmed by NPD. The spectra are quite complex below 90 K, it is very difficult to extract any information due to strong peak broadening in addition to the large number of overlapping subspectra. Given the complexity of the structure, four oxidation states spread over four crystallographic sites, possible impurities due to the second magnetic phase (k_2) and the eventuality of having to solve the full Hamiltonian for Fe^{2+}, it was not possible to obtain an unambiguous fit of the 4 K spectrum.

4. Conclusion

This low temperature study of the stoichiometric "114" $YBaFe_4O_{7.0}$ oxide shows for the first time the appearance of long-range magnetic ordering in the $LnBaFe_4O_{7.0}$ series. A novel form of $YBaFe_4O_{7.0}$, with a monoclinic structure is obtained below 180 K, which corresponds to the distortion of the cubic high temperature and then of the tetragonal room temperature forms successively. The monoclinic distortion allows a lifting of the geometrical frustration induced by the topology the $[Fe_4]_\infty$ sublattice in the cubic structure. This explains the difference of magnetic behavior between the air exposed $YBaFe_4O_{7+\delta}$, that keeps the cubic symmetry down to 4 K and exhibits a spin glass behaviour, while an antiferromagnetic ordering below 95 K is observed in the oxygen stoichiometric $YBaFe_4O_{7.0}$ distorted structure.

It is worth pointing out that the atomic displacements that are involved in the structural transitions of $YBaFe_4O_{7.0}$, show that the oxygen atoms of the YO_6 octahedra are mainly directed toward the barium atoms as the symmetry decreases, tending to compensate the underbonding of barium. Thus, the latter seems to be a key parameter for the appearance of structural distortions and consequently for the generation of magnetic ordering. Remarkably, the magnetic structure of this monoclinic phase also suggests the possibility of charge ordering as supported by Mössbauer data. Nevertheless, the values of magnetic moments of iron, smaller than the theoretical values, due to the coexistence of magnetic frustration, will require a further detailed study, using Mössbauer spectroscopy in order to confirm this statement. Single crystal investigations should also be carried out to better understand the magnetic and transport properties of $YBaFe_4O_{7.0}$.

This study also points out that, despite their different structures, the hexagonal based $YBaCo_4O_{7+\delta}$-type and cubic based $YBaFe_4O_{7+\delta}$-type oxides can be considered as one family: the "114" compounds. As a matter of fact, similar to $YBaCo_4O_{7+\delta}$-type "114" oxides, the magnetism of $YBaFe_4O_{7+\delta}$ is mainly governed by a competition between magnetic frustration and magnetic ordering. For these two related structures, the stabilization of the high symmetry forms by insertion of even slight quantities of oxygen ($\delta>0$) results in a magnetically frustrated behavior, whereas the structural transitions of the stoichiometric compounds ($\delta=0$) lift the geometrical frustration resulting in long range ordering of the spins. Moreover, the barium underbonding was found to be the driving parameter of the structural distortions in both cases, confirming the similarities of the structure-properties relationships in that family of compounds.

Acknowledgment

The authors acknowledge H. Zheng and J. Mitchell for useful discussions and their comments on this present paper. The authors acknowledge the CNRS, the Ministère de l'Enseignement Supérieur et de la Recherche and the Conseil Regional of Basse Normandie for financial support in the frame of Emergence Program and FCT, Portugal, project PTDC/CTM-CER/114561/2009 and grant PTDC/CTM/64357/2006. V. P. acknowledges support by the ANR-09-JCJC-0017-01 (Ref: JC09_442369). V. D. and B. R. acknowledge Dr. A. Pautrat and F. Veillon for their assistance with measurements.

References

[1] M. Valldor, M. Andersson, Solid State Sci. 4 (2002) 923–931.
[2] L. Chapon, P. Radaelli, H. Zheng, J. Mitchell, Phys. Rev. B: Condens. Matter 74 (2006) 172401.
[3] N. Nakayama, T. Mizota, Y. Ueda, A.N. Sokolov, A.N. Vasiliev, J. Magn. Magn. Mater. 300 (2006) 98–100.
[4] A. Huq, J.F. Mitchell, H. Zheng, L.C. Chapon, P.G. Radaelli, K.S. Knight, P.W. Stephens, J. Solid State Chem. 179 (2006) 1136–1145.
[5] M. Soda, Y. Yasui, T. Moyoshi, M. Sato, N. Igawa, K. Kakurai, J. Magn. Magn. Mater. 310 (2007) e441–e442.
[6] D.D. Khalyavin, L.C. Chapon, P.G. Radaelli, H. Zheng, J.F. Mitchell, Phys. Rev. B: Condens. Matter 80 (2009) 144107.
[7] M. Markina, A.N. Vasiliev, N. Nakayama, T. Mizota, Y. Yeda, J. Magn. Magn. Mater. 322 (2010) 1249–1250.
[8] A.I. Rykov, Y. Ueda, M. Isobe, N. Nakayama, T.P. Yu, S.A. Petrov, A.N. Shmakov, V.N. Kriventsov, A.N. Vasiliev, New J. Phys. 12 (2010) 043035.
[9] E.A. Juarez-Arellano, A. Friedrich, D.J. Wilson, L. Wiehl, W. Morgenroth, B. Winkler, M. Avdeev, R.B. Macquart, C.D. Ling, Phys. Rev. B: Condens. Matter 79 (2009) 064109.
[10] V. Caignaert, V. Pralong, V. Hardy, C. Ritter, B. Raveau, Phys. Rev. B: Condens. Matter 81 (2010) 094417.
[11] V. Caignaert, V. Pralong, A. Maignan, B. Raveau, Solid State Commun. 149 (2009) 453–455.
[12] V. Caignaert, A.M. Abakumov, D. Pelloquin, V. Pralong, A. Maignan, G. Van Tendeloo, B. Raveau, Chem. Mater. 21 (2009) 1116–1122.
[13] S. Avci, O. Chmaissem, H. Zheng, A. Huq, D.D. Khalyavin, P.W. Stephens, M.R. Suchomel, P. Manuel, J.F. Mitchell, Phys. Rev. B: Condens. Matter 85 (2012) 094414.
[14] A. Maignan, V. Caignaert, D. Pelloquin, S. Hébert, V. Pralong, J. Hejtmanek, D. Khomskii, Phys. Rev. B: Condens. Matter 74 (2006) 165110.
[15] V. Pralong, V. Caignaert, A. Maignan, B. Raveau, J. Mater. Chem. 19 (2009) 8335.
[16] V. Duffort, V. Caignaert, V. Pralong, N. Barrier, B. Raveau, M. Avdeev, H. Zheng, J.F. Mitchell, J. Solid State Chem. 191 (2012) 225–231.
[17] P. Karen, A. Kjekshus, J. Am. Ceram. Soc. 77 (1994) 547–552.
[18] J.C. Waerenborgh, D.P. Rojas, N.P. Vyshatko, A.L. Shaula, V.V. Kharton, I.P. Marozau, E.N. Naumovich, Mater. Lett. 57 (2003) 4388–4393.
[19] H. Rietveld, J. Appl. Crystallogr 2 (1969) 65–71.
[20] J. Rodríguez-Carvajal, Physica B 192 (1993) 55–69.
[21] J.M. Perez-Mato, D. Orobengoa, M.I. Aroyo, Acta Crystallogr., Sect. A: Found. Crystallogr. 66 (2010) 558–590.
[22] D. Orobengoa, C. Capillas, M.I. Aroyo, J.Manuel Perez-Mato, J. Appl. Crystallogr 42 (2009) 820–833.
[23] M.I. Aroyo, J.M. Perez-Mato, C. Capillas, E. Kroumova, S. Ivantchev, G. Madariaga, A. Kirov, H. Wondratschek, Z. Kristallogr.—–Cryst. Mater. 221 (2006) 15–27.
[24] A. Le Bail, Powder Diffr 20 (2005) 316–326.
[25] J.B. Goodenough, Phys. Rev. 117 (1960) 1442–1451.
[26] T. Rudolf, K. Ch, F. Mayr, J. Hemberger, V. Tsurkan, A. Loidl, New J. Phys. 9 (2007) 76.
[27] K. Kuo, C.W. Cheng, G. Chern, J. Appl. Phys 111 (2012) 07A507-3.
[28] H. Ueda, Y. Ueda, Phys. Rev. B: Condens. Matter 77 (2008) 224411.
[29] V. Caignaert, A. Maignan, V. Pralong, S. Hébert, D. Pelloquin, Solid State Sci. 8 (2006) 1160–1163.
[30] M. Karppinen, H. Yamauchi, S. Otani, T. Fujita, T. Motohashi, Y.H. Huang, M. Valkeapää, H. Fjellvåg, Chem. Mater. 18 (2006) 490–494.
[31] H. Hao, X. Zhang, Q. He, C. Chen, X. Hu, Solid State Commun. 141 (2007) 591–594.
[32] H. Hao, C. Chen, L. Pan, J. Gao, X. Hu, Physica B 387 (2007) 98–102.
[33] A. Maignan, V. Caignaert, V. Pralong, D. Pelloquin, S. Hébert, J. Solid State Chem. 181 (2008) 1220–1226.
[34] W. Wong-Ng, W. Xie, Y. Yan, G. Liu, J. Kaduk, E. Thomas, T. Tritt, J. Appl. Phys. 110 (2011) 113706–113708.
[35] J.C. Waerenborgh, E.V. Tsipis, L.C.J. Pereira, M. Avdeev, E.N. Naumovich, V.V. Kharton, Dalton Trans. 41 (2012) 667–678.
[36] N.N. Greenwood, T.C. Gibb, Mossbauer Spectroscopy, Chapman and Hall, Ltd. Publisher, London, 1971.
[37] J. Lindén, P. Karen, J. Solid State Chem. 183 (2010) 2703–2713.
[38] P. Karen, K. Gustafsson, J. Lindén, J. Solid State Chem. 180 (2007) 148–157.
[39] J. Lindén, P. Karen, H. Yamauchi, M. Karppinen, J. Magn. Magn. Mater. 272–276 (2004) E267–E268, Supplement.